https://doi.org/10.5194/egusphere-2025-4548
Preprint. Discussion started: 20 February 2026
© Author(s) 2026. CC BY 4.0 License.

Implementation of the Generalized Double-Moment Scaling Normalization Method for Raindrop Size Distribution in a WRF 4.3.1 Bulk-Type Cloud Microphysics Scheme: A Case Study over the Korean Peninsula

Joonghyun Jo[1], Kyo-Sun Sunny Lim[1,2*], Sun-Young Park[2], Juhee Kwon[3], Wonbae Bang[2], HyangSuk Park[4], Jae-Young Byon[4], Hyun-Suk Kang[4], and Gyuwon Lee[1,2 *]

[1]BK21 Weather Extremes Education & Research Team, Department of Atmospheric Sciences, Kyungpook National University, Republic of Korea

[2]Center for Atmospheric REmote sensing (CARE), Kyungpook National University, Republic of Korea

[3] Research Institute of Basic Sciences, Seoul National University, Seoul, Korea

[4]Forecast Research Department, National Institute of Meteorological Sciences, Korea Meteorological Administration, Republic of Korea

* Corresponding Author: K.-S. S. Lim (kyosunlim@knu.ac.kr); Gyuwon Lee (gyuwon@knu.ac.kr)

https://doi.org/10.5194/egusphere-2025-4548
Preprint. Discussion started: 20 February 2026
© Author(s) 2026. CC BY 4.0 License.

Abstract

This study is the first to adopt the Generalized Double-Moment scaling Normalization (GDMN) method to represent the rain Drop Size Distribution (DSD) in a bulk-type cloud microphysics scheme, specifically the Weather Research and Forecasting (WRF) Double-moment 6-class (WDM6) scheme. The modified scheme, referred to as WDM6-GDMN, is evaluated through simulations of an isolated summer convection case over the Korean Peninsula, using the universal double-moment normalized DSD function, $h(x)$, derived from rain DSDs observed in the Boseong region during the summers of 2018 and 2019. WDM6-GDMN provides a more realistic spatial distribution of surface precipitation by better simulating convection-cell movement. Although none of the cloud microphysics parameterizations, including the bin-type scheme, reproduce the observed convection that developed in the southeast of the analysis domain, only WDM6-GDMN successfully captures this feature. Microphysical analysis demonstrates that, in WDM6-GDMN, enhanced cloud production due to stronger upward motion leads to the formation of more raindrops and, consequently, greater surface precipitation over southeastern region. Furthermore, the contoured frequency by altitude diagrams for the WDM6-GDMN reveals slower particle growth and weaker reflectivity in the lower atmosphere compared with the original scheme, in better agreement with observations.

1. Introduction

Bulk-type cloud microphysics schemes adopt a specific functional form of the Drop Size Distribution (DSD) for each hydrometeor type (e.g., cloud water, rain, cloud ice, snow, and graupel/hail), rather than calculating the evolution of the DSD at each diameter bin (Lin et al., 1983; RH1983; Ferrier, 1994; Meyers et al., 1997; Reisner et al., 1998; Morrison, 2005; P3, 2015; Thompson, 2008; Milbrandt and Yau, 2011). This approach to representing DSD evolution is computationally efficient, meaning that bulk-type cloud microphysics schemes can be applied to operational numerical or climate models. Among several microphysics schemes, the Weather Research and Forecasting (WRF) Double-moment 6-class (WDM6) bulk microphysics scheme (Lim and Hong, 2010) has been widely used across regions for research and operational purposes (Byun et al., 2011; Gao et al., 2011; Morrison et al., 2015; Lim et al., 2020).

Previous studies have shown that the WDM6 scheme tends to overestimate reflectivity, as demonstrated by contoured frequency by altitude diagram (CFAD) analyses (Min et al., 2015; Chakraborty et al., 2021). Min et al. (2015) evaluated the performance of the WRF Single-Moment 6-class (WSM6) and WDM6 cloud microphysics schemes using radar observations during summer season. They reported that although the WDM6 agrees better with radar observations than WSM6, both schemes overestimate the height of the melting level and the bright band relative to observations, as revealed by CFAD analysis. Additionally, WDM6 tends to overestimate reflectivity below the melting layer during summer monsoon cases. Chakraborty et al. (2021) compared WDM6 with other microphysics schemes, including the WSM6, Milbrandt, and Thompson Aerosol-aware schemes. They found that WDM6 tends to retain precipitation hydrometeors rather than precipitating them immediately, leading to greater accumulation of frozen hydrometeors in the upper layers. In the same study, CFAD analysis revealed that WDM6 produces the strongest reflectivity in the upper and middle levels among the microphysics schemes. suggesting unrealistic precipitation growth in the ice-phase region above the melting layer.

The WDM6 scheme adopts a rain DSD in the form of a generalized gamma distribution with a fixed shape parameter (μ), following the study by Cohard and Pinty (2000). Although most bulk microphysics schemes employ a fixed shape parameter, several observational studies have reported that the rain DSD shape parameter varies considerably (Yang et al., 2019; Uijlenhoet et al., 2003; Dolan et al., 2018; Cha et al., 2022; Lee et al. 2023). Yang et al. (2019) showed that the rain DSD shape parameter proposed by Testud et al. (2001) ranges from –2.3 to 60 over southern England during 2013–2017.

https://doi.org/10.5194/egusphere-2025-4548
Preprint. Discussion started: 20 February 2026
© Author(s) 2026. CC BY 4.0 License.

Furthermore, they found that increasing the shape parameter initially leads to an underestimation of rainfall, followed by an overestimation. Uijlenhoet et al. (2003) noted that the rain DSD shape parameter varies depending on the stage of precipitation development and the type of convection (e.g., stratiform or convective). Dolan et al. (2018) analysed 12 disdrometer datasets spanning three latitude bands—high (≥ 45°N), middle (23°N–45°N), and low (≤ 23°N)—and various precipitation types, including light rain, orographic precipitation, deep convection, organized midlatitude systems, and tropical oceanic rainfall. They found that the mean shape parameter values of rain observed using a two-dimensional video disdrometer (2DVD), Joss-Waldvogel disdrometer (JWD), and automated particle size velocity (PARSIVEL) units (APU) vary by region, ranging from –1.20 to 7.26. Similarly, Cha et al. (2022) compared DSD parameters observed with JWD and PARSIVEL across nine regions in Korea and East Asia and reported mean shape parameter values ranging from –0.158 to 8.37. These findings indicate that using a fixed shape parameter in the gamma DSD model is not optimal and that more representative values should be applied.

Scaling normalization is commonly employed to represent the hydrometeor DSD and has been extensively studied since the 1990s (Sempere-Torres et al., 1994; Testud et al., 2001; Lee et al., 2004; Berne et al., 2012; Morrison et al., 2019; Lee et al. 2023). Sempere-Torres et al. (1994) performed the first scaling normalization of DSDs based on a single reference variable, the rainfall rate (R). Later, Testud et al. (2001) extended this single normalization to a double-moment normalization using the third and fourth moments of the DSD. They showed that the mean raindrop volume diameter (D_m) exhibits significant variability, while the intercept parameter (N_0^*) shows no correlation with R. Lee et al. (2004) further demonstrated that the normalization approach of Testud et al. (2001) can only represent a specific case that uses the third and fourth moments. To address this limitation, Lee et al. (2004) generalized the normalization concept and proposed a general form of double-moment scaling normalization, $N(D)/\ N_0' = h(D/D_\mathrm{m}')$, where the generalized characteristic number density (N_0') and generalized characteristic diameter (D_m') can be defined using any combination of two moments. The Generalized Double-Moment scaling Normalization (GDMN) significantly reduces the scatter in the normalized DSD compared to single-moment normalization and decrease the standard deviation of the fractional error in the n-th moment estimation, leading to a more accurate representation of the DSD.

Berne et al. (2012) compared the temporal and spatial variability of DSDs using the single-moment normalization method of Sempere-Torres et al. (1994) and the GDMN method of Lee et al. (2004) over the École Polytechnique Fédérale de Lausanne (EPFL) during March 2009 and July 2010. They figured out that GDMN better represents the temporal and spatial variability of DSDs. The GDMN method can be also successfully applied to the retrieval of spatiotemporally varying DSDs from dual-polarimetric radar measurement (Kwon et al. 2020; Lee et al. 2023; Shin et al. 2024). Meanwhile, Morrison et al. (2019) extended the GDMN analysis by comparing triple-moment normalization with single- and double-moment normalization using disdrometer data obtained from the U.S. Department of Energy (DOE) Atmospheric Radiation (ARM) program sites worldwide. They noted that increasing the number of reference moments can reduce variability in the DSD parameters.

To evaluate the applicability of the GDMN method for representing the DSD in a bulk-type cloud microphysics scheme, this study develops a new version of WDM6, termed WDM6-GDMN, by incorporating the GDMN approach to represent the rain DSD, following Lee et al. (2004). The performance of WDM6-GDMN is examined through simulations of an isolated summer convection event using observed normalized DSD functions. Section 2 outlines the proposed method, Section 3 describes the experimental setup, case study, and observational data, and Sections 4 and 5 present the results and the summary and conclusions, respectively.

2. Generalized Double-Moment scaling Normalization (GDMN) method

https://doi.org/10.5194/egusphere-2025-4548
Preprint. Discussion started: 20 February 2026
© Author(s) 2026. CC BY 4.0 License.

2.1 Original Rain Drop Size Distribution (DSD) in WDM6

The original WDM6 scheme adopts the gamma form of the DSD for rain with a static shape parameter of c and μ, as shown in Eq. (1):

$$N_{\mathrm{R}}(D_{\mathrm{R}}) = N_{0\mathrm{R}}\,(D_{\mathrm{R}})^{c\mu-1}\exp\{-(\lambda_{\mathrm{R}}D_{\mathrm{R}})^{c}\}. \quad (1)$$

Where c and μ have values of 1 and 2, respectively; $N_{\mathrm{R}}(D_{\mathrm{R}})$, with a unit of m^{-4}, is the number concentration corresponding to the rain diameter (D_{R}), which has units m; and $N_{0\mathrm{R}}$ and λ_{R} denote the intercept and slope parameters of the rain DSD, which have units of $\mathrm{m}^{-3-c\mu}$ and m^{-1}, respectively, and can be expressed by the following equations:

$$N_{0\mathrm{R}} = N_{\mathrm{R}}\frac{c}{\Gamma(\mu)}(\lambda_R)^{c\mu}, \quad (2)$$

$$\lambda_{\mathrm{R}} = \left[\frac{\pi\rho_R}{6}\frac{N_R}{\rho_a q_R}\frac{1}{q_{\mathrm{R}}}\frac{\Gamma(\mu+\frac{d_{\mathrm{R}}}{c})}{\Gamma(\mu)}\right]^{\frac{1}{d_{\mathrm{R}}}}, \quad (3)$$

where q_{R} and N_{R} represent the rain mixing ratio and number concentration, respectively, with units of kg kg^{-1} and m^{-3}; ρ_{R} and ρ_{a} are the density of the rain and air, respectively, with units of kg m^{-3}; and d_{R} is the parameter used in the calculation of the mass (M)–diameter (D) relationship ($M = c_{\mathrm{R}}D^{d_{\mathrm{R}}}$). Since raindrops are assumed to be spherical in WDM6, d_{R} has a value of 3. It is noteworthy that the unit of $N_{0\mathrm{R}}$ is nonphysical and depends on the two shape parameters, c and μ, expressed as $\mathrm{m}^{-3-c\mu}$.

2.2 New DSD adopting the GDMN method

The DSD can be formulated as the product of the zeroth moment and a probability density function, and the following GDMN is then derived from the assumption of multiple power-law relationships among moments (Lee et al., 2004).

$$N(D) = N_0' h(D/D_{\mathrm{m}}'), \quad (4)$$

where N_0' and D_{m}' are the generalized characteristic number density and the generalized characteristic diameter, with units of m^{-4} and m, respectively. They can be defined using any combination of two moments, as follows:

$$N_0' = M_i^{(j+1)/(j-i)}M_j^{(i+1)/(i-j)}, \quad (5)$$

$$D_{\mathrm{m}}' = (M_j/M_i)^{\frac{1}{j-i}}, \quad (6)$$

where i and j denote the moment order, and M_i and M_j represent the i-th and j-th moments of the DSD, respectively, which are calculated as $M_i = \int N(D)D^i dD$. The $h(x)$ in Eq. (4) is the normalized DSD based on the two moments, M_i and M_j, where $x = D/D_{\mathrm{m}}'$. It should be noted that no assumption on the functional form of $h(x)$ is applied. Thus, this GDMN can be applied to any observed DSD if the multiple power-law relationship is satisfied.

When the GDMN method is applied to the generalized gamma DSD, the normalized DSD takes the non-dimensional form $h(x)$.

$$h_{\mathrm{GG}(i,j,\mu,c)}(x) = c\Gamma_i^{(j+c\mu)/(i-j)}\Gamma_j^{(-i-c\mu)/(i-j)}x^{c\mu-1}\exp\left[-\left(\frac{\Gamma_i}{\Gamma_j}\right)^{c/(i-j)}x^c\right], \quad (7)$$

where $\Gamma_i = \Gamma(\mu + i/c)$ and $\Gamma_j = \Gamma(\mu + j/c)$. The subscript GG($i$, j, μ, c) in $h(x)$ denotes the generalized gamma DSD, and i, j, μ, and c in the parenthesis indicate the i-th and j-th moments and shape parameters. The advantage of expressing the DSD as $h(x)$ (Eq. (4)) is that it provides a comprehensive framework to represent any naturally occurring DSD, while $h(x)$ remains

https://doi.org/10.5194/egusphere-2025-4548
Preprint. Discussion started: 20 February 2026
© Author(s) 2026. CC BY 4.0 License.

relatively stable and less variable because most of significant variability is explained by the two reference moments (Lee et al., 2004).

2.3 Incorporation of GDMN method for rain DSD in WDM6

Recognizing the importance of rain-related microphysical processes such as collision–coalescence and raindrop breakup in precipitation initiation, storm intensity, and cold-pool dynamics (Lim and Hong, 2012; Morrison et al., 2012; Hagos et al., 2015), this study introduces the first application of the GDMN method to the rain DSD in the WDM6 scheme. To apply the GDMN method of Lee et al. (2004) in WDM6 using the zeroth (i = 0) and third (j = 3) moments, which are the prognostic variables of rain in WDM6, the original rain DSD ($N_R(D_R)$) and rain diameter (D_R) must be normalized by $N_0' = (M_0^4/M_3)^{\frac{1}{3}}$ and $D_m' = (M_3/M_0)^{\frac{1}{3}}$ (Eqs. (5) and (6)). With this normalization, the rain DSD can be rewritten as Eq. (8):

$$N_R(D_R) = N_0' \, h_{GG(0,3,\mu,c)}(D_R/D_m'), \tag{8}$$

where $h_{GG(0,3,\mu,c)}(x_R)$ with $x_R = D_R/D_m'$ can be expressed as Eq. (9):

$$h_{GG(0,3,\mu,c)}(x_R) = \frac{c}{\Gamma(\mu)}\left(\frac{\Gamma\left(\mu+\frac{3}{c}\right)}{\Gamma(\mu)}\right)^{\frac{c\mu}{3}} x_R^{c\mu-1}\exp\left[-\left\{\left(\frac{\Gamma\left(\mu+\frac{3}{c}\right)}{\Gamma(\mu)}\right)^{\frac{1}{3}}(x_R)\right\}^c\right]. \tag{9}$$

The original WDM6 scheme employs fixed shape parameters, $c = 1$ and $\mu = 2$, for the gamma DSD in Eq. (1), resulting in the form $N(D) = N_0 D\exp\{-\lambda D\}$. Furthermore, instead of treating c and μ separately, the original WDM6 adopts a single parameter, $\mu_R = c\mu - 1$. This implies that μ_R remains unchanged whether c=1, μ=2 or c=2, μ=1. As shown by Lee et al. (2004, 2023), the variability of DSDs, arising from changes in number concentration, mean diameter, and shape, can be substantially reduced through scaling normalization. Variations in the shape parameters c and μ have only a minor effect to the normalized DSD, $h(x)$, which therefore becomes stable and nearly universal. The universal $h(x)$ function provides a more effective representation of DSD variability, as implemented in WDM6-GDMN.

2.4 Microphysics

The WDM6 cloud microphysics parameterization scheme predicts the mixing ratios of six hydrometeor types (water vapor, cloud water, cloud ice, rain, snow, and graupel) as well as the total number concentrations of cloud water, rain, and cloud condensation nuclei. Figure 1 presents a flowchart of the WDM6 scheme, illustrating the various microphysical processes among hydrometeors. By applying the GDMN method, $N_R(D_R)$ is expressed in terms of $h_{GG(0,3,\mu,c)}(x_R)$, as shown in Eq. (8). Consequently, the parameterization of 16 rain-related microphysical processes must to be re-derived: nine associated with mixing-ratio predictions and seven with total number concentration predictions. Fourteen of these processes are indicated by green boxes in Figure 1, excluding the two processes related to sedimentation of the rain mixing ratio and its number concentration. A list of the symbols used in this study is provided in Appendix A.

Figure 1: Flowchart of the microphysical processes for the prediction of (a) mixing ratios and (b) number concentrations in the WDM6 scheme (Lim and Hong, 2010). The terms in red (blue) are activated when the temperature is above (below) 0 °C, whereas the terms in black occur across the entire temperature range. The green rectangles represent newly re-derived microphysics processes.

https://doi.org/10.5194/egusphere-2025-4548
Preprint. Discussion started: 20 February 2026
© Author(s) 2026. CC BY 4.0 License.

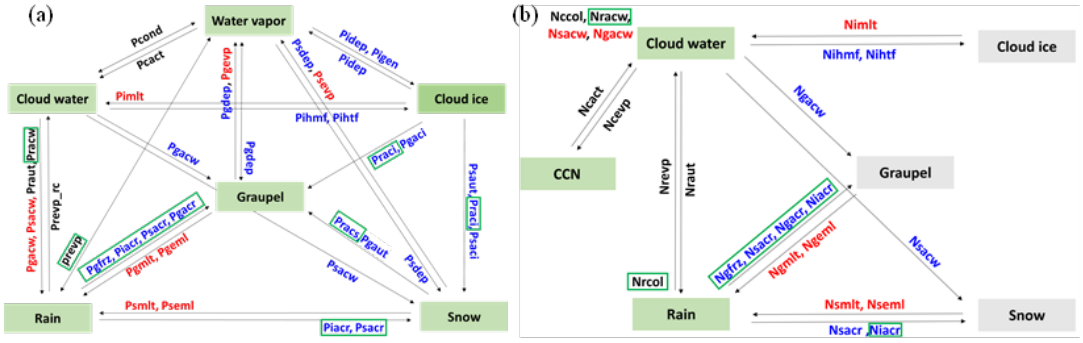

3. Experimental setup

3.1 Case description and model setup

Song and Sohn (2015) classified summer rainfall events over the Korean Peninsula into two types: cold-type and warm-type. Cold-type events, driven by convective instability, are typically locally developed and short-lived, making them difficult to accurately simulate in numerical models. Compared with warm-type events, cold-type rainfall exhibits stronger convective instability, allowing clouds to develop to higher altitudes and producing more intense rainfall. In this study, one cold-type summer rainfall event that occurred on 6 August 2013 is analysed to test the impact of applying the GDMN method to the rain DSD within WDM6 scheme. The selected event exhibited the highest frequency of lightning strikes over the heavy precipitation area during summer of 2013–2018.

Figure 2: (a) Surface synoptic chart at 03:00 UTC on 6 August 2013, and (b) 15-h accumulated surface precipitation (mm) during the analysis period (02:00-17:00 UTC on 6 August 2013), obtained from the Korea Meteorological Administration (KMA) Automatic Weather Station (AWS) network. The red dots in (b) indicate the locations of the Kwanaksan (KWK) and Gwangdeuksan (GDK) radar sites used to validate simulated radar reflectivity. The red solid line from A to B denotes the transect for cross-sectional analysis, while the red dashed box indicates the area used for microphysical process analysis. The red triangle marks the Boseong standard weather observatory, where a two-dimensional video disdrometer (2DVD) was installed to observe rain drop size distributions (DSDs).

https://doi.org/10.5194/egusphere-2025-4548
Preprint. Discussion started: 20 February 2026
© Author(s) 2026. CC BY 4.0 License.

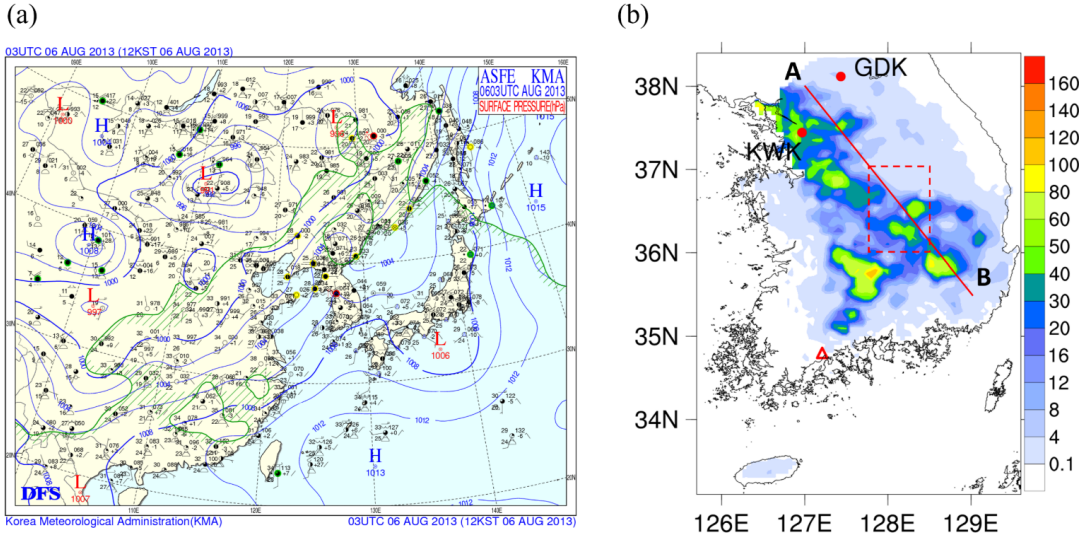

Figure 3: The model domain, consisting of three nested domains with resolutions of 9 km (d01), 3 km (d02), and 1 km (d03). Shading indicates the terrain height in meters above sea level. The analysis domain is denoted by the black dotted line within the innermost domain (d03).

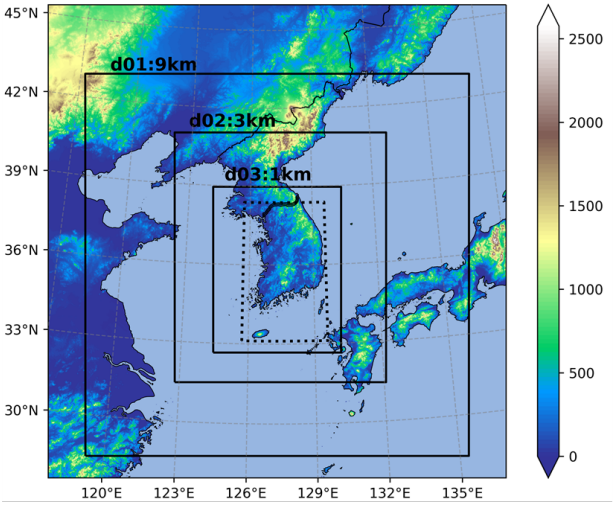

The model forecast spans the period from 23:00 UTC on 05 August 2013 to 17:00 UTC on 6 August 2013, with the analysis period defined as 02:00-17:00 UTC on 6 August 2013. Version 4.3.1 of the WRF model (Skamarock et al., 2019) is employed, with three nested domains as horizontal resolutions of 9, 3, and 1 km, as shown in Figure 3. All domains have 65 vertical levels, with time steps of 45, 15, and 5 seconds for domains 1 (d01), 2 (d02), and 3 (d03), respectively. The physics parameterizations include the Kain–Fritsch cumulus scheme for D01 only (Kain and Fritsch, 1990; Kain, 2004), the Revised MM5 Monin–Obukhov surface layer scheme (Jiménez et al., 2012), the Unified Noah land surface scheme (Chen and Dudhia 2001), the Rapid Radiative Transfer Model for General Circulation Models (RRTMG) for both longwave and shortwave radiation (Iacono et al., 2008; Morcrette et al., 2008), and the Yonsei University planetary boundary layer scheme (Hong et

https://doi.org/10.5194/egusphere-2025-4548
Preprint. Discussion started: 20 February 2026
© Author(s) 2026. CC BY 4.0 License.

al., 2006). The European Centre for Medium-Range Weather Forecasts (ECMWF) Reanalysis 5 (ERA5) dataset (Hersbach et al., 2020) provides the initial and boundary conditions. The model configuration and physical parameterizations for each domain are summarized in Table 1.

195

Table 1. A summary of the Weather Research and Forecasting (WRF) model configuration and references for all physics schemes except for the cloud microphysics scheme.

	WRF V4.3.1			References
	Domain 1	Domain 2	Domain 3	
Grid number (x x y x y)	180 x 180 x65	295 x 349 x65	532 x 691 x65	
Horizontal resolution	9 km	3 km	1 km	
Cumulus parameterization	Kain-Fritsch	No cumulus	No cumulus	Kain and Fritsch (1990), Kain (2004)
Surface layer	Revised MM5 Monin–Obukhov scheme			Jiménez et al. (2012)
Land surface	Unified Noah land surface model			Chen and Dudhia (2001)
Longwave and shortwave radiation	Rapid Radiative Transfer Model for General Circulation Models			Iacono et al. (2008)
Planetary Boundary Layer	Yonsei University scheme			Hong et al. (2006)
Initial/boundary data	ERA5 (fifth generation ECMWF reanalysis product)			Hersbach et al. (2020)

3.2 Observation Data and Numerical Experiments

200

Radar reflectivity observed from two the Kwanaksan (KWK) and Gwangdeuksan (GDK) sites was analysed using Contoured Frequency by Altitude Diagrams (CFADs; Fig. 2), which illustrate the frequency of occurrence of reflectivity values at various heights. The CFAD analysis is used to evaluate the impact of incorporating the GDMN method into the WDM6 scheme on the vertical structure of reflectivity. Reflectivity is examined within a 100 km radius of each radar site. The KWK
205 and GDK radars provide data at 10-minute intervals, whereas both the original WDM6 and the modified WDM6-GDMN schemes produce outputs at 1-hour intervals. To enable a direct one-to-one temporal comparison between the radar and model results, radar data collected within 30 minutes before and after each hour were compared with the corresponding hourly model outputs.

The WDM6-GDMN allows the observed shape parameters, c and μ, to be applied to the rain DSD. To calculate c
210 and μ from observed rain DSDs over the Korean Peninsula, data from a 2DVD are utilized. The 2DVD is widely recognized as a reference instrument for the large end of the DSD but has been shown to underestimate the concentrations of small drops (Raupach et al., 2018), which significantly affects M_0. Consequently, it is not appropriate to derive $h_{\mathrm{GG}(0,3,\mu,c)}(x)$ directly from observed DSDs by normalizing with the zeroth and third moments. Therefore, this study follows two steps to obtain $h_{\mathrm{GG}(0,3,\mu,c)}(x)$. Normalization is first performed using N_0' and D_{m}', defined with the third and fourth moments, M_3 and M_4, for
215 the observed rainfall events (threshold: $R \geq 0.1$ mm h^{-1}) at the Boseong standard weather observatory during 2018 and 2019 (Fig. 2b). Then, $h_{\mathrm{GG}(3,4,\mu,c)}(x)$ is derived from the mean $h(x)$ by minimizing $\sum(\log h_{\mathrm{mean}}(x) - \log h(x))^2$ (Bang et al., 2020).

https://doi.org/10.5194/egusphere-2025-4548
Preprint. Discussion started: 20 February 2026
© Author(s) 2026. CC BY 4.0 License.

Where $h_{\mathrm{med}}(x)$ is the channel-wise median of the normalized DSDs. By applying this approach, the train DSD, $N_{\mathrm{R}}(D)$, can be derived from $h_{GG(3,4,\mu,c)}(x)$, $N_0'(M_3, M_4)$, and $D_{\mathrm{m}}'(M_3, M_4)$, by applying the observed parameters c=2.70 and μ=0.24 at the Boseong site for the third and fourth moments as follows:

$$N_{\mathrm{R}}(D)/(\mathrm{m}^{-4}) = N_0'(M_3, M_4)\, h_{\mathrm{GG}(3,4,\mu,c)}(D/D_{\mathrm{m}}'(M_3, M_4)). \quad (12)$$

The calculated $N_{\mathrm{R}}(D)$ is then normalized by ${N_0}'(M_0, M_3)$ and ${D_{\mathrm{m}}}'(M_0, M_3)$, where M_0 and M_3 are derived from $N_{\mathrm{R}}(D)$. The normalized DSDs, $h(x)$, are presented as a frequency distribution in Figure 4. Finally, $h_{\mathrm{GG}(0,3,\mu,c)}(x)$ is obtained by minimizing the value of $\sum(\log h_{\mathrm{med}}(x) - \log h(x))^2$. The derived shape parameters c and μ are 2.60 and 0.29, respectively, for $h_{\mathrm{GG}(0,3,\mu,c)}(x)$.

Figure 4: Normalized DSD derived from $N_0'(M_0, M_3)$ and $D_{\mathrm{m}}'(M_0, M_3)$, along with their $h_{\mathrm{med}}(x)$ over the Boseong area. Colors indicate the normalized frequency of the DSD. The solid line represents $h_{\mathrm{med}}(x)$ for each channel.

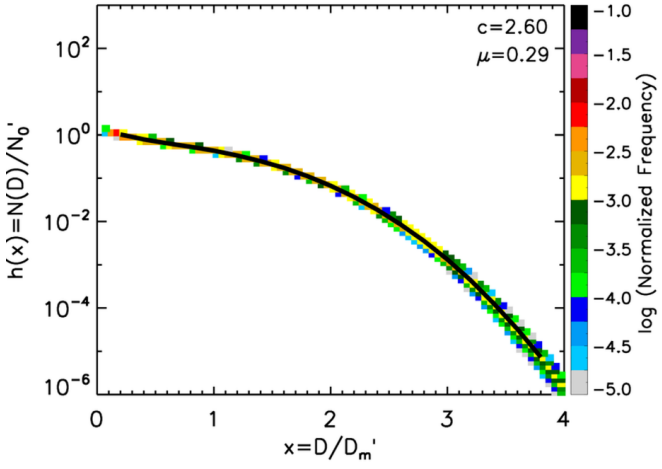

To examine the effect of the GDMN method on the rain DSD in simulated convection, two experiments, named WDM6 and GDMN, are conducted for the selected case. WDM6 uses the shape parameters c=1 and μ=2 in the rain DSD, expressed by the gamma function as in the original WDM6 scheme. GDMN applies the WDM6-GDMN (see Section 2) with the observed shape parameters of c=2.60 and μ=0.29 (Fig. 4). To further evaluate simulated precipitation across different cloud microphysics schemes, additional experiments are conducted using three other double-moment bulk-type microphysics schemes—Morrison, Thompson, Predicted Particle Properties (P3) —as well as the simplified Spectral Bin-type Microphysics (SBM) scheme.

4. Results

Figure 5 shows the observed radar reflectivity at 06:00, 07:00, and 08:00 UTC on 6 August 2013, along with the simulated radar reflectivity from the WDM6 and GDMN experiments. The Column Maximum (CMAX) observations at 06:00 UTC reveal two distinct regions of strong reflectivity (Fig. 5a): one over the northwestern Korean Peninsula, which moves south-eastward over time, and another, consisting of a smaller convection cell, in the south of the peninsula, moving eastward (Figs. 5a–c). By 08:00 UTC, these two convection cells converge, producing strong reflectivity over the southeastern Korean

https://doi.org/10.5194/egusphere-2025-4548
Preprint. Discussion started: 20 February 2026
© Author(s) 2026. CC BY 4.0 License.

Peninsula (Fig. 5c). The WDM6 scheme does not reproduce this movement accurately, especially for the northwestern system. Although the initial stages of the two precipitation cells in WDM6 are similar to the observations (Figs. 5a and d), the stronger northwestern cell fails to move south-eastward, shifting mostly eastward instead (Figs. 5d–f). As a result, the two precipitation cells move eastward independently and do not merge, as observed. Conversely, GDMN reproduces the movement of the two precipitation cells more realistically (Figs. 5g–i). Although weak reflectivity signals remain over the western Korean Peninsula, the two cells merge in GDMN, producing intense reflectivity over the southeastern peninsula at 08:00 UTC, consistent with observations (Figs. 5g–i).

Figure 5: The spatial distribution of maximum reflectivity (dBZ) at 06:00 UTC (left), 07:00 UTC (middle), and 08:00 UTC (right) on 6 August 2013 from (a–c) the Column Maximum (CMAX) radar observation, (d–f) WDM6, and (g–i) GDMN.

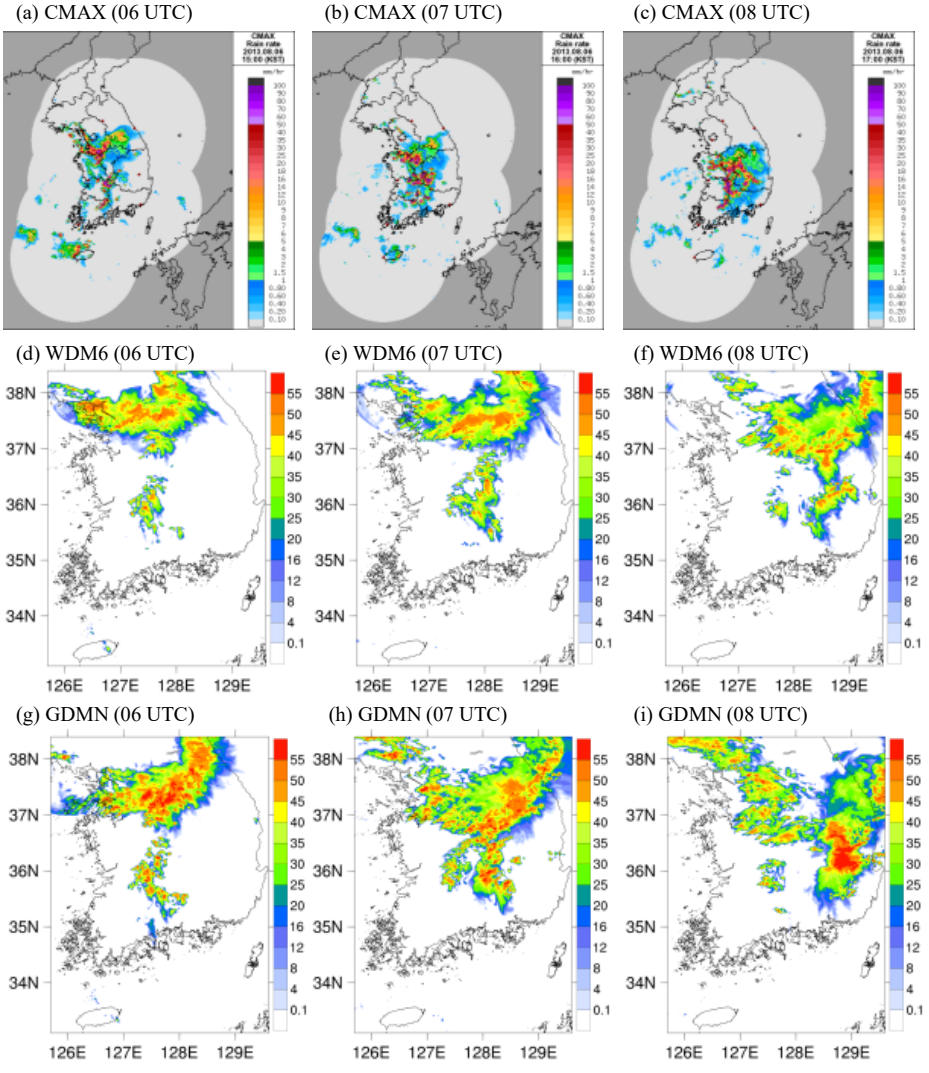

https://doi.org/10.5194/egusphere-2025-4548
Preprint. Discussion started: 20 February 2026
© Author(s) 2026. CC BY 4.0 License.

The spatial distribution of cumulative surface precipitation on 6 August 2013 is shown in Figure 6a and b. Compared with AWS observations, WDM6 overestimates precipitation over the northeastern Korean Peninsula and underestimates it in the west and south (Fig. 6c). In WDM6, precipitation cells approaching from the northwest move eastward, leading to excessive surface precipitation in the northeast. In contrast, GDMN produces more precipitation in the southeast due to the merging of two precipitation cells in that area, thereby reducing the bias of WDM6 relative to AWS (Fig. 6d). This reduction in bias is attributed to GDMN's more accurate simulation of the movement of precipitation cells initially located in the northwest. To quantify the spatial distribution of accumulated surface precipitation, statistical skill scores—including Root Mean Square Error (RMSE), Bias, Probability of Detection (POD), False Alarm Ratio (FAR), and Equivalent Threat Score (ETS)—are calculated for WDM6 and GDMN (Table 2). Although GDMN underestimates total surface precipitation relative to observations, all statistical skill scores show improvement compared with WDM6.

Figure 6: Accumulated surface precipitation (mm) during the analysis period (from 02:00 to 17:00 UTC on 6 August 2013) for (a) WDM6, (b) GDMN, and (c) the difference between WDM6 and Automatic Weather Station (AWS) observations (WDM6 minus AWS). (d) Same as (c), but for the difference between GDMN and WDM6 (GDMN minus WDM6).

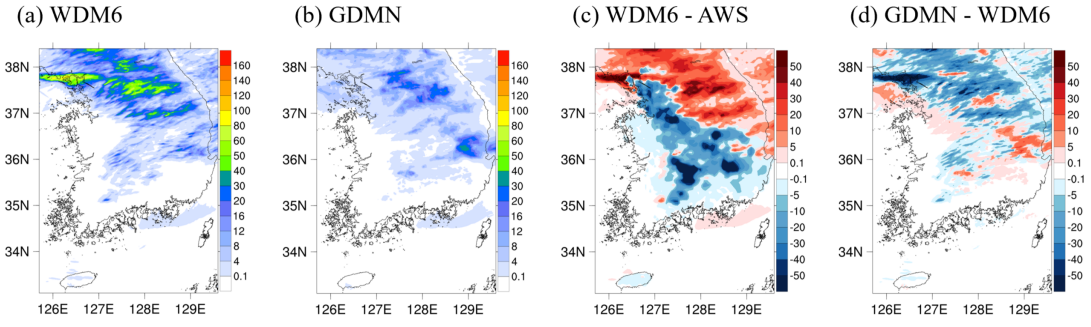

Table 2. Statistical skill scores for the simulated precipitation over the analysis domain during the analysis period: Root Mean Square Error (RMSE), Bias, Probability of Detection (POD), False Alarm Ratio (FAR), and Equivalent Threat Score (ETS).

	RMSE	BIAS	POD	FAR	ETS
WDM6	6.72	2.0	0.16	0.70	0.05
GDMN	5.03	1.39	0.18	0.68	0.07

To further evaluate the performance of GDMN method, CFADs from the KWK and GDK sites are analysed for two simulations (Fig. 7). The location of the two sites used in the CFAD analysis are shown in Figure 2b. The highest precipitation during the analysis period was recorded at KWK, whereas only a small amount was observed at GDK, despite the model simulations indicating substantial precipitation at this site. In Figure7, the x-axis represents reflectivity, the y-axis represents altitude, and the colour scale indicates the frequency ratios (%) at specific altitudes and reflectivity values. The reflectivity values range from 5 to 60 dBZ. Black solid lines denote the cumulative reflectivity frequencies at the 25th, 50th, and 75th percentiles.

At KWK, between 10 and 12 km in altitude, weak reflectivity values of approximately 6-7 dBZ are frequently observed, gradually increasing toward 4 km, where precipitation particles grow. The median reflectivity below 4 km is about 20 dBZ. In WDM6, the reflectivity is generally overestimated relative to radar observations. No distinct melting layer is simulated, and the increase in reflectivity with decreasing altitude down to the 4 km is similar to observations. However,

https://doi.org/10.5194/egusphere-2025-4548
Preprint. Discussion started: 20 February 2026
© Author(s) 2026. CC BY 4.0 License.

between 6 and 10 km, the increase occurs more rapidly than in the observations. WDM6 produces a median reflectivity of 30 dBZ below 4 km, about 10 dBZ higher than radar observations, and frequently reproduces strong reflectivity exceeding 40 dBZ. In contrast, GDMN exhibits a slower increase in reflectivity with decreasing altitude compared with WDM6, making it closer to observations. GDMN shows a bright-band signature at 5 km and a decrease in reflectivity near the surface, indicating possible substantial evaporation in the lower layers.

For the GDK site, peak reflectivity is observed at 4 km, indicating the presence of a distinct melting layer at this altitude. Radar observations also show gradually increasing reflectivity from 12 to 4 km, similar to the KWK site, followed by a decrease from 4 km to the surface. In WDM6, reflectivity increases rapidly from the top to 4 km, and the bright band is not distinctly simulated. This rapid increase in reflectivity, inconsistent with observations, was also noted in Min et al. (2015), indicating improper growth of solid particles in the WDM6 scheme. Additionally, WDM6 overestimates reflectivity below 4 km by about 10 dBZ compared with radar observations. In contrast, GDMN simulates a clear bright band at around 4 km, with a median reflectivity of 35 dBZ. Particle growth in GDMN is much slower than in WDM6 over the upper layers, consistent with observations. GDMN also reproduces a clear trend of decreasing reflectivity below the melting layer at GDK. Overall, GDMN produces a more realistic bright-band signature at the GDK site and a more accurate representation of solid-particle growth than WDM6 at both sites.

Figure 7: Contoured Frequency by Altitude Diagram percentiles at the KWK and GDK radar sites (location shown in Fig. 2b) for (a) radar observations, (b) WDM6, and (c) GDMN at the KWK site during the analysis period. Panels (d)–(f) are the same as (a)–(c) but at the GDK site. Solid lines denote the cumulative reflectivity frequencies at the 25th, 50th, and 75th percentiles.

https://doi.org/10.5194/egusphere-2025-4548
Preprint. Discussion started: 20 February 2026
© Author(s) 2026. CC BY 4.0 License.

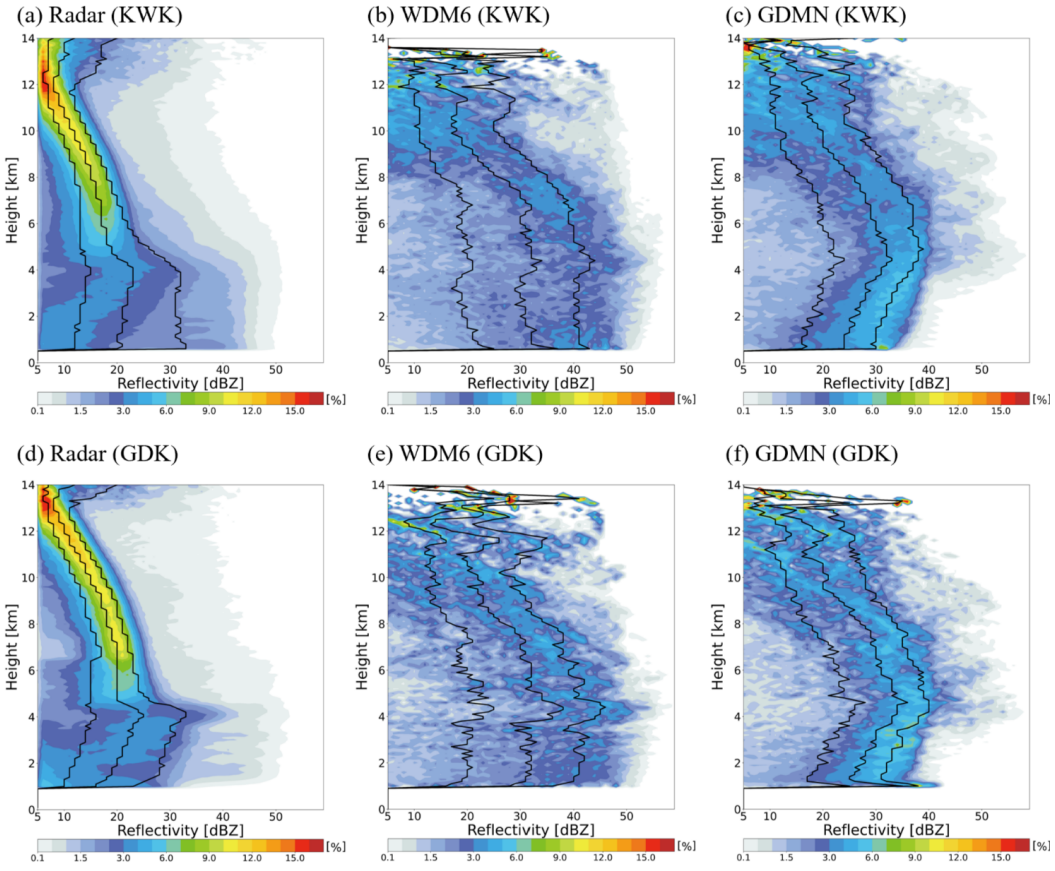

Figure 8 shows the 1-hour accumulated surface precipitation along the cross-section shown in Figure 2b from 04:00 to 08:00 UTC on 6 August. The cross-section spans the path of the precipitation cell, which AWS observations show was initially located over the northwestern Korean Peninsula and moved south-eastward over time (Fig. 2b). This movement is well simulated in GDMN but not captured in WDM6 (Fig. 5d–i). In both WDM6 and GDMN, precipitation begins to develop in the northwest (Location "A" in Fig. 8) after 04:00 UTC (Fig. 8a) and gradually shifts south-eastward (Location "B" in Fig, 8) with time (Fig. 8b–d). WDM6 simulates a persistent precipitation peak near "A" from 04:00 to 06:00 UTC failing to capture the south-eastward movement of precipitation cells (Fig. 5). By contrast, in GDMN, the precipitation peak shifts from Area A to Area B between 04:00 to 08:00 UTC (Figs. 8a–d). Between 05:00 and 06:00 UTC, the maximum precipitation location in GDMN is similar to that in WDM6; however, it subsequently shifts markedly south-eastward. The difference between the two schemes arises from GDMN's more realistic representation of precipitation cell movement.

Figure 8: 1-hour accumulated surface precipitation along the cross-sectional area indicated by the red solid line in Fig. 2b for (a) 04:00 to 05:00 UTC, (b) 05:00 to 06:00 UTC, (c) 06:00 to 07:00 UTC, and (d) 07:00 to 08:00 UTC on 6 August 2013. Black and blue lines represent WDM6 and GDMN, respectively.

https://doi.org/10.5194/egusphere-2025-4548
Preprint. Discussion started: 20 February 2026
© Author(s) 2026. CC BY 4.0 License.

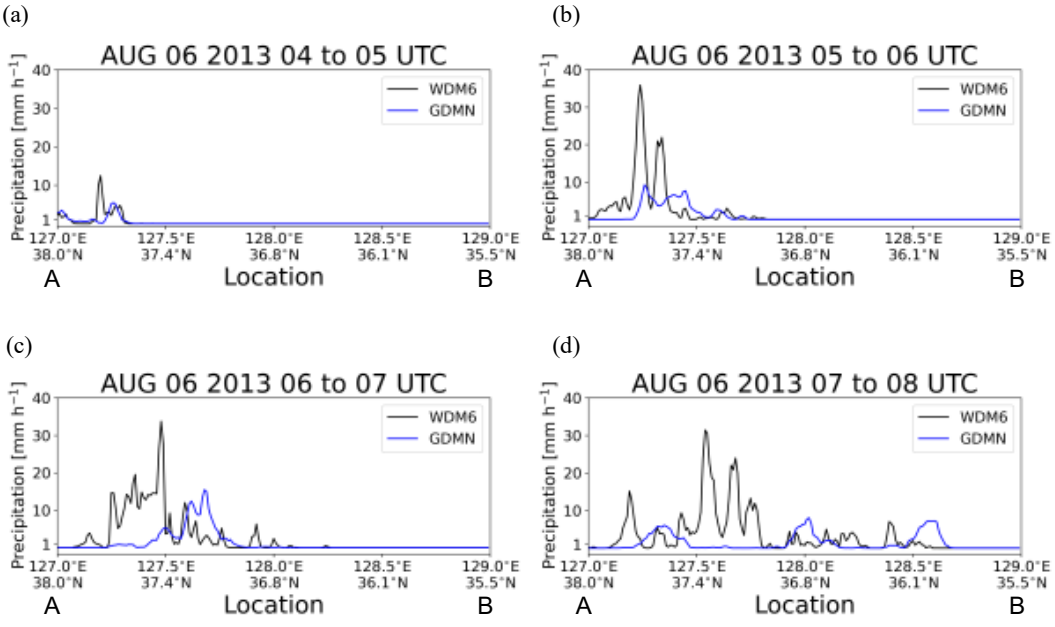

To identify the main causes of the differences in simulated precipitation and reflectivity between GDMN and WDM6, thermodynamic fields and mixing ratios are further analysed in Figures 9 and 10, focusing on 07:00 and 08:00 UTC, when two precipitation cells merged into a single cell. Figure 9 presents the vertical structures of temperature and wind along the cross-sectional area shown in Figure 2b. In WDM6, a strong updraft develops near 37.3° N at 07:00 UTC and dissipates by 08:00 UTC, producing intense precipitation at the same location during this hour (Figs. 9a and 8d). As the precipitation cells originating in the northwest move eastward, the updraft driving the convection at 07:00 UTC is no longer visible at 08:00 UTC. In contrast, GDMN simulates an updraft farther southeast, near 36.5° N at 07:00 UTC (Fig. 9a and c). The south-eastward-moving precipitation cell merges with the eastward-moving cells and continues moving south-eastward, maintaining an updraft near 35.5° N at 08:00 UTC (Fig. 9d). Additionally, GDMN produces a colder environment below 1 km compared with WDM6, (Fig. 9). The stronger and more extensive near-surface cooling in GDMN drives the precipitation cells south-eastward, whereas the relatively weak near-surface cold environment in WDM6 limits the south-eastward propagation of the system.

Figure 9: Temperature with terrain along the cross-section indicated by the red line in Fig. 2b at (a) 07:00 UTC, (b) 08:00 UTC on 6 August 2013 for WDM6. Panels (c) and (d) are the same as (a) and (b), but for GDMN. The wind fields are overlaid at the corresponding times. Red contour lines indicate 20 dBZ reflectivity.

https://doi.org/10.5194/egusphere-2025-4548
Preprint. Discussion started: 20 February 2026
© Author(s) 2026. CC BY 4.0 License.

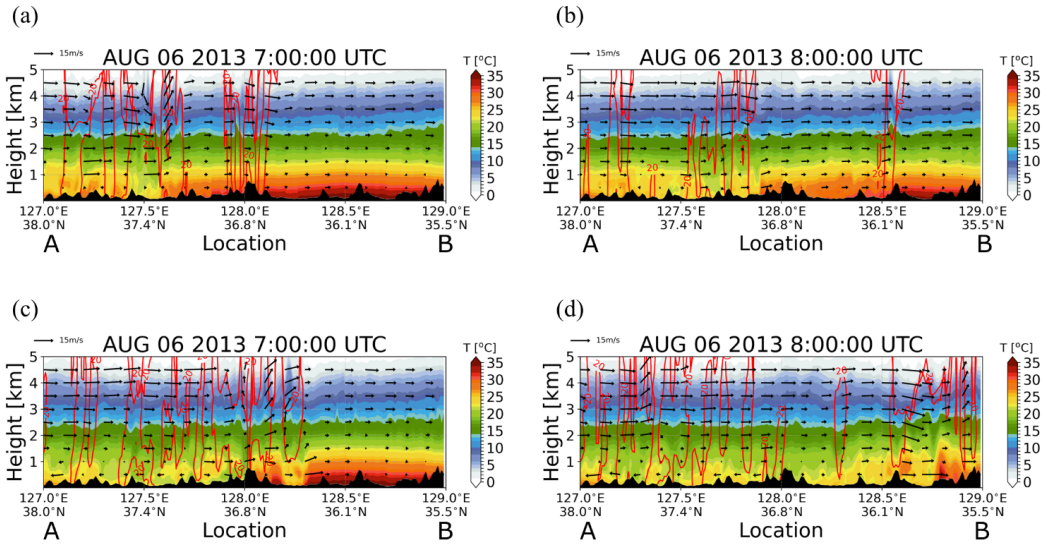

Figure 10: Differences (GDMN – WDM6) in (a) temperature (°c), (c) cloud mixing ratio (g kg^{-1}), and (e) rain mixing ratio (g kg^{-1}), shown with terrain (black color) along the cross-section indicated by the red line in Fig. 2b at 07 UTC 6 August 2013. Panels (b), (d), and (f) show the same fields as (a), (c), and (e), respectively, at 08 UTC.

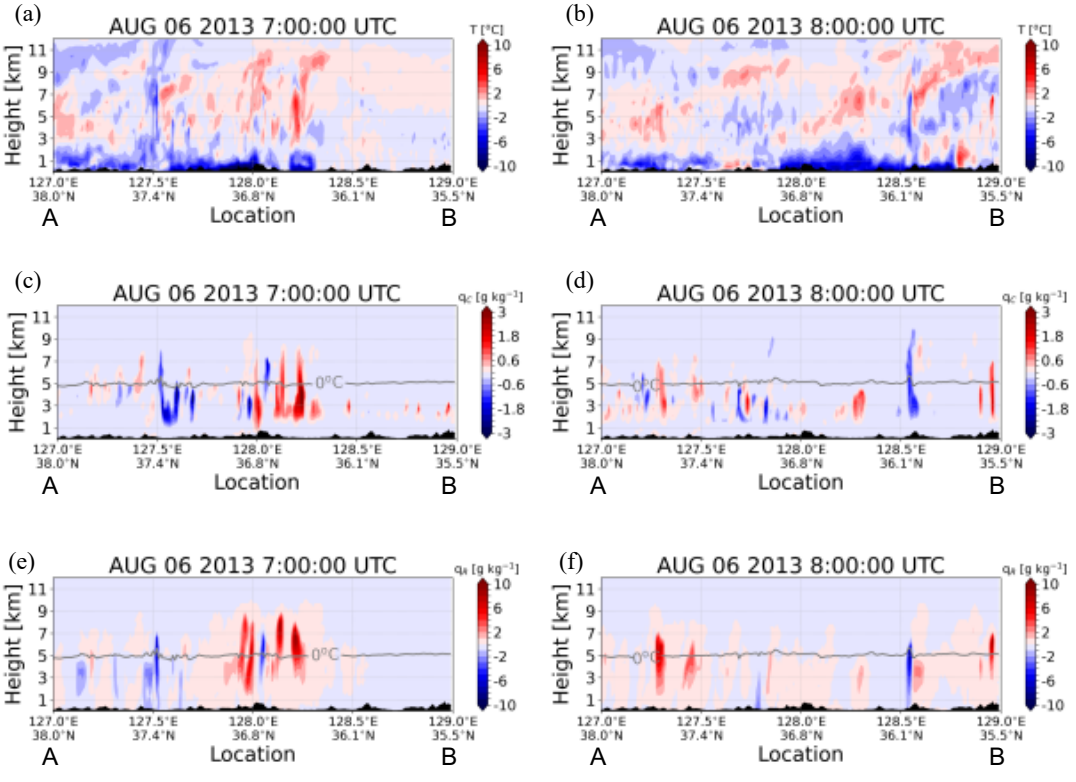

https://doi.org/10.5194/egusphere-2025-4548
Preprint. Discussion started: 20 February 2026
© Author(s) 2026. CC BY 4.0 License.

At 07:00 and 08:00 UTC, compared to WDM6, GDMN exhibits stronger cooling in the lower layer behind the precipitation cells (Fig. 10a and 10b). The differences in cloud and rain mixing ratios between GDMN and WDM6 show a similar trend. At 07:00 UTC, the cloud mixing ratio increases significantly near 36.5° N in GDMN, coinciding with a region of strong updrafts and an enhanced rain mixing ratio (Fig. 10c and 10e). A comparable pattern is observed around 35.5° N at 08:00 UTC (Fig. 10d and 10f), where vigorous upward motion generates a supersaturated environment, leading to cloud formation and, consequently, precipitation both aloft and at the surface.

Figure 11 shows the differences (GDMN minus WDM6) in the time-area averaged vertical distribution of prognostic hydrometeor mixing ratios (cloud water (q_C), cloud ice (q_I), rain (q_R), snow (q_S), and graupel (q_G)) and number concentrations (cloud condensation nuclei (N_N), cloud water (N_C), and rain (N_R)). Below 9 km, both the rain mixing ratio and the number concentration are significantly higher in GDMN compared to WDM6. In addition, GDMN exhibits slightly higher cloud water mixing ratios and number concentrations below 6 km, as well as greater graupel mixing ratios above 3 km. The enhanced graupel production in GDMN is likely a consequence of stronger convective updrafts in the model.

Figure 11: Differences in the time-domain averaged vertical distribution (GDMN minus WDM6) over the region denoted by the red dashed box in Fig. 2b for (a) mixing ratio (g kg^{-1}) and (b) number concentration (m^{-3}) between 06:00 and 08:00 UTC on 6 August 2013.

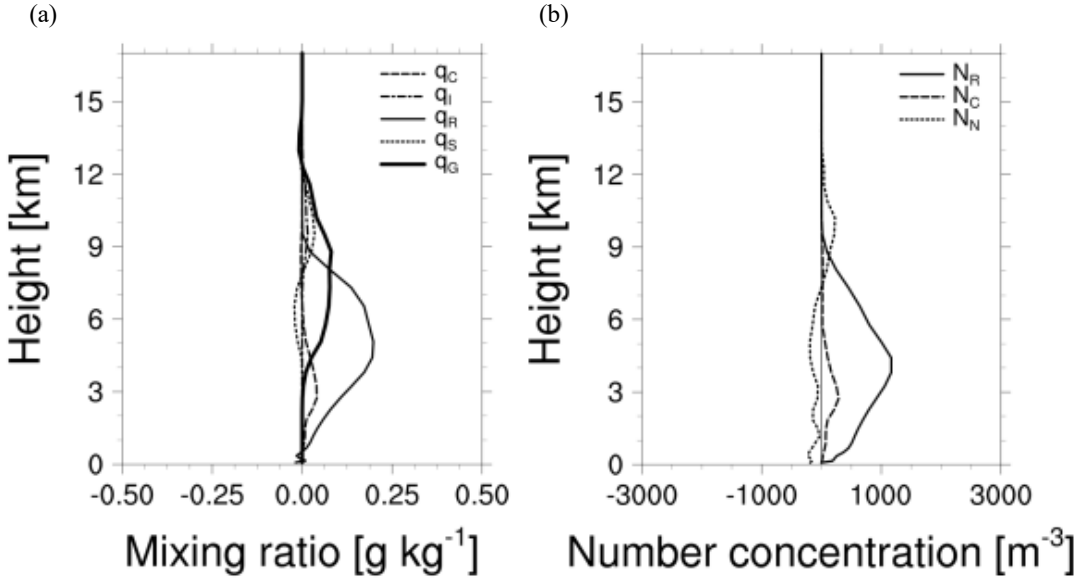

To identify the microphysical processes responsible for the increased generation of rain and cloud water in GDMN compared to WDM6, the vertical profiles of the time-area averaged major source and sink terms for the rain and cloud mixing ratios are analysed in Figure 12. In GDMN (solid line), the condensation process of water vapor into cloud water (Pcond) is enhanced below 9 km relative to WDM6 (dashed line) under saturated conditions, serving as the primary source of the cloud mixing ratio (Fig. 12a). The higher cloud mixing ratio in GDMN also intensifies accretion with rain (Pracw) (Fig. 12b), which acts not only the main sink of cloud water but also the main source of rain (blue solid line in Fig. 12c). Among the major

https://doi.org/10.5194/egusphere-2025-4548
Preprint. Discussion started: 20 February 2026
© Author(s) 2026. CC BY 4.0 License.

sources of rain, Pracw produces a greater rain mixing ratio in GDMN than in WDM6. Moreover, graupel melting (Pgmlt), the second-largest source of the rain mixing ratio, is higher in GDMN owing to greater graupel production. The larger rain content in GDMN further increases ascending rain, which subsequently enhances graupel formation through raindrop freezing (Pgfrz) and accretion of rain by graupel (Pgacr) (Fig. 12d). Notably, rain evaporation (Prevp) is the primary sink of rain in the lower atmosphere, particularly below 5 km. Enhanced Prevp in GDMN compared to WDM6 leads to increased evaporation of rain into water vapor, cooling the lower atmosphere. As a result, precipitation cells in GDMN tend to propagate south-eastward, consistent with the observed behaviour.

Figure 12: The vertical profiles of the time-domain averaged (a) sources and (b) sinks of the cloud mixing ratios (g kg^{-1} s^{-1}) over the region indicated by the red dashed box in Fig. 2b between 06:00 and 08:00 UTC on 6 August 2013. Only the major microphysical processes are represented. The solid and dashed lines represent GDMN and WDM6, respectively. Panels (c) and (d) show the same as (a) and (b) but for the rain mixing ratio (g kg^{-1} s^{-1}).

https://doi.org/10.5194/egusphere-2025-4548
Preprint. Discussion started: 20 February 2026
© Author(s) 2026. CC BY 4.0 License.

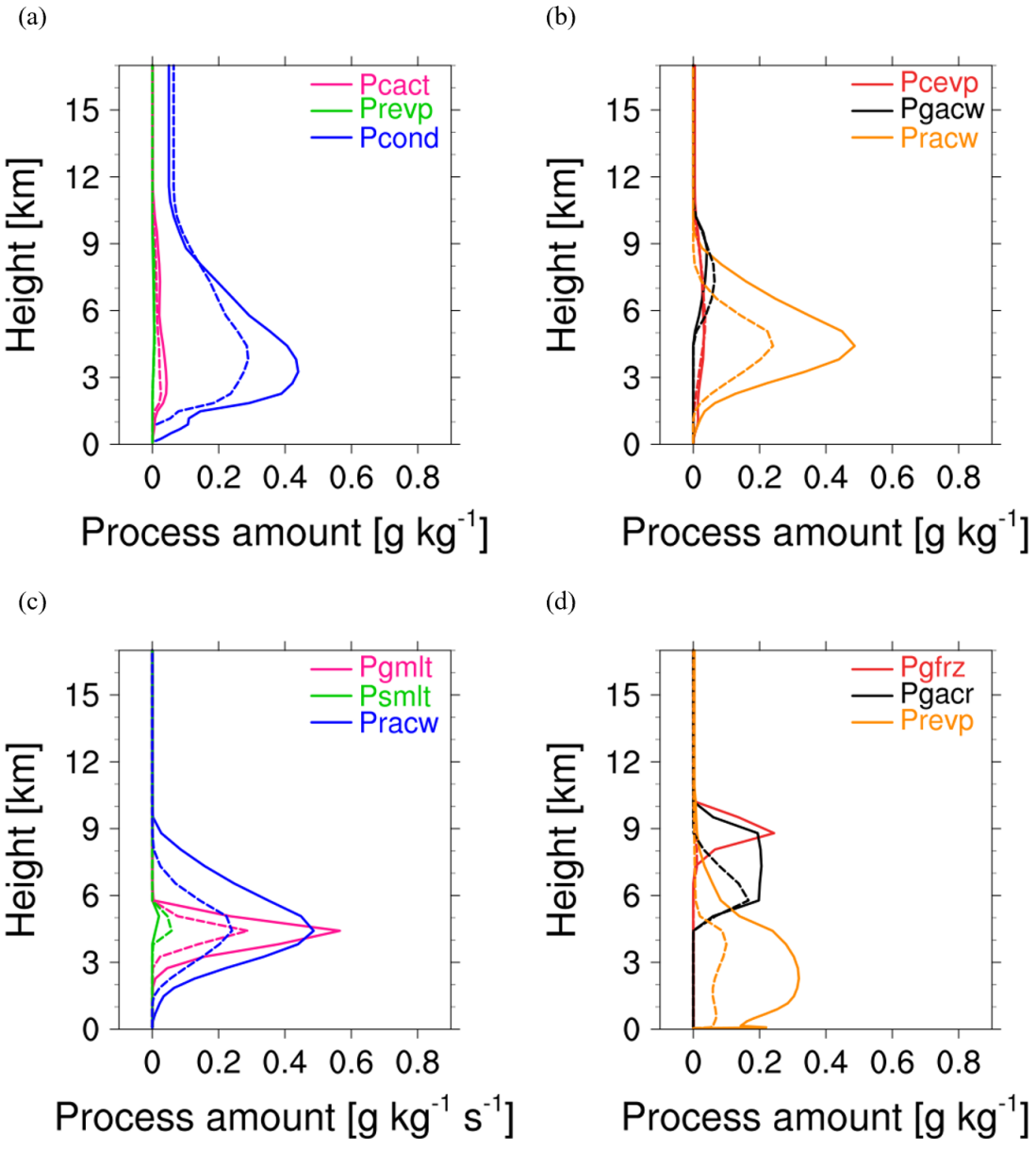

385

5. Summary and Discussion

This study applies the Generalized Double-moment scaling Normalization (GDMN) method to parameterize the rain drop size distribution (DSD) in the WDM6 microphysics scheme, which originally represent the DSD using
390 a gamma distribution. By adopting the GDMN method, the variability of the DSD more effectively captured, thereby reducing uncertainties of DSD. The 0th and 3rd moments are used to represent the DSD within GDMN, and sixteen microphysical processes related to rain reformulated. Long-term observed rain shape parameter values (c=2.6,

https://doi.org/10.5194/egusphere-2025-4548
Preprint. Discussion started: 20 February 2026
© Author(s) 2026. CC BY 4.0 License.

μ=0.29), calculated from 2DVD data collected over the Boseong area during May-October of 2018 and 2019, are applied to the DSD through the GDMN method in WDM6. Numerial experiments are conducted for a cold-type summer rainfall event characterized by strong convection.

The results demonstrate that incorporating GDMN into the WDM6 scheme alleviates limitation of the original WDM6 scheme, which misrepresents precipitation cell propagation and produces accumulated precipitation patterns that deviate from observations. In the modified scheme, precipitation cells move south-eastward and subsequently collide with another cell generated within the Korean Peninsula, leading to increased precipitation in the southeastern regions. Overall, the modified WDM6 reproduces a more realistic propagation of precipitation cells and a more accurate spatial distribution of accumulated surface precipitation than the original scheme, achieving higher scores across all statistical skill metrics for surface precipitation.

To evaluate the simulated vertical reflectivity structure, CFAD analysis is performed using data from two radar sites, KWK and GDK. The original WDM6 scheme exhibits excessively rapid particle growth between the upper and middle layers (4–5 km) and consistently overestimate reflectivity at all altitudes. In contrast, the modified WDM6 scheme produces more gradual particle growth from the top to the middle layers, with significantly reduced reflectivity, resulting in better agreement with observed patterns. These results indicate that the modified rain DSD influences not only warm-rain microphysical processes but also mixed-phase ones, including accretion between liquid- and solid-phase particles. Consequently, the simulated reflectivity in the upper layer us more realistically represented.

Thermodynamic analysis along the path of cell movement reveals that the modified WDM6 scheme successfully triggers convective updrafts over the southeastern Korean Peninsula, which are absent in the original WDM6 scheme. In the modified WDM6, enhanced condensation of water vapor into cloud water over the updraft region increases cloud formation and promotes the production of numerous small raindrops through collision–coalescence and graupel melting. Furthermore, the modified WDM6 simulates a relatively cooler lower environment due to stronger rain evaporation, which enhances near-surface cooling. This intensified cooling drives the south-eastward propagation of precipitation cells, consistent with observations.

None of the bulk or bin microphysics schemes analysed in this study accurately reproduce the observed precipitation distribution across the Korean Peninsula on 6 Augst 2013 (Figs. 13 and 2b). All simulations employing bulk-type cloud microphysics schemes, which adopt a gamma DSD with constant shape parameters, generate spatial precipitation patterns similar to the original WDM6, with excessive precipitation over the central–eastern Korean Peninsula compared to AWS observations (Figs. 13a-c). The prescribed DSD function and fixed shape parameters in these schemes constrain their ability to realistically simulate precipitation. Tapiador et al. (2025) emphasized that the DSD strongly influences the physical properties of precipitation systems, including total surface area and scattering characteristics, and highlighted the need for DSD modelling to be grounded in a physically consistent framework in which drop shapes follow an appropriate probability density function (PDF). Even the SBM scheme, which explicitly predicts the particle size distribution, fails to reproduce the observed spatial distribution of accumulated precipitation (Fig. 13d).

Our study demonstrates the advantage of applying the revised rain DSD using the GDMN method within the WDM6 scheme for simulating isolated deep convection events that develop during the summer season over the Korean peninsula. Although this work evaluates only a single convection case, the merits of the GDMN method are evident when compared simulations using more advanced microphysics schemes, such as the P3 scheme and the bin-type schemes. Future work will extend the GDMN approach to prescribe the DSDs of other hydrometeors and to evaluate its performance across a wider range of precipitation systems.

https://doi.org/10.5194/egusphere-2025-4548
Preprint. Discussion started: 20 February 2026
© Author(s) 2026. CC BY 4.0 License.

Figure 13: The accumulated surface precipitation (mm) on 6 August 2013 using (a) Morrison, (b) Thompson, (c) P3, and (d) SBM cloud microphysics schemes.

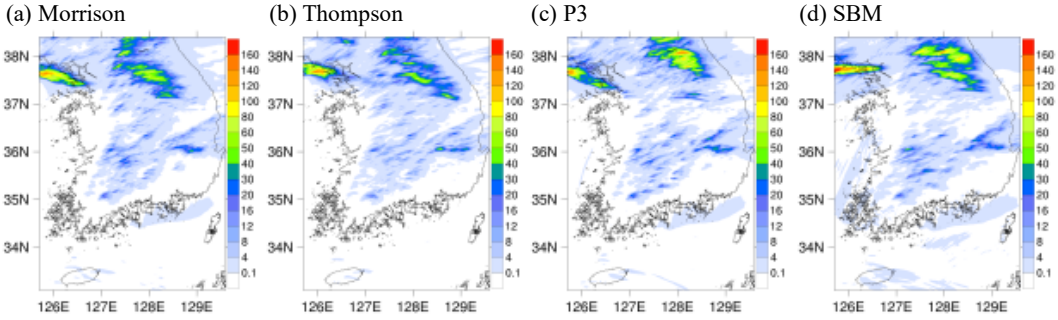

Code and data availability. The WRF Model version 4.3.1 and the input files required for model integration are available at https://doi.org/10.5281/zenodo.18328177. Initial and boundary conditions are provided from the ERA5 reanalysis data at 6-hour intervals, available at https://cds.climate.copernicus.eu/datasets/reanalysis-era5-single-levels?tab=overview and https://cds.climate.copernicus.eu/datasets/reanalysis-era5-pressure-levels?tab=overview. ERA5 single-level and pressure-level fields at 6-hour intervals are used, with the initial time set to 23 UTC on 5 August 2013. For the pressure-level variables, all vertical levels are included. The model codes for WDM6 and GDMN experiments with the scripts for figures in this manuscript can be found in https://doi.org/10.5281/zenodo.17194841 and https://doi.org/10.5281/zenodo.18346989. The AWS and radar data used for the analysis are available at https://doi.org/10.5281/zenodo.18328177. The output data for four additional microphysics schemes (Thompson, Morrison, P3, and SBM) used for comparison with the WDM6 and GDMN experiments are also available at https://doi.org/10.5281/zenodo.18346989.

Author contributions. JJ conducted the model simulations and performed the data analysis under the supervision of KL and GL. The manuscript was written by KL, JJ, and GL with substantial input from all co-authors. WB processed the DSD observational dataset. KL and other authors contributed to scientific discussions and provided constructive feedback.

Competing interests. The authors declare that they have no conflict of interest.

Funding. This work was funded by the Korea Meteorological Administration Research and Development Program "Observing Severe Weather in Seoul Metropolitan Area and Developing Its Application Technology for Forecasts" under Grant (KMA2018-00125).

Acknowledgments. The authors would like to thank the participants of the field campaign "Korea Precipitation Observation Program: international collaborative experiments for Mesoscale convective system in Seoul metropolitan area" (KPOP-MS), hosted by the Korea Meteorological Administration (KMA).

https://doi.org/10.5194/egusphere-2025-4548
Preprint. Discussion started: 20 February 2026
© Author(s) 2026. CC BY 4.0 License.

Appendix A: List of symbols

Symbol	Meaning	Value	SI unit
c	Shape parameter of the rain		
c_R	Empirical formula of M_R	$\pi\rho_R/6$	
D	Diameter		m
D'_m	Generalized characteristic diameter	$(M_j/M_i)^{\frac{1}{j-i}}$	m
D_R	Rain diameter		m
d_R	Empirical formula of M_R	3	
I	The number of moment		
j	The number of moment		
M_i	I-th moment		
M_j	J-th moment		
M_0	0th moment		m^{-3}
M_3	Third moment		
$M_R(D_R)$	Mass of rain of diameter D_R		kg
$N_R(D_R)$	Number concentration corresponding to the diameter of rain (D_R).		m^{-3}
$N(D)$	Number concentration corresponding to the diameter (D).		m^{-3}
N_{0R}	Intercept parameter of rain	8×10^6	m^{-4}
N'_0	Generalized characteristic number concentration	$M_i^{(\frac{j+1}{j-i})} M_j^{(\frac{i+1}{i-j})}$	m^{-4}
N_R	Number concentration of rain		m^{-3}
q_R	Mixing ratio of rain		
Γ	Gamma function		
λ_R	Slope of rain size distribution		m^{-1}
μ	Shape parameter of the rain		
π	Pi	3.14	
ρ_0	Density of air at reference state	1.28	kg m^{-3}
ρ_a	Air density		kg m^{-3}
ρ_R	Density of rain	1000	kg m^{-3}

https://doi.org/10.5194/egusphere-2025-4548
Preprint. Discussion started: 20 February 2026
© Author(s) 2026. CC BY 4.0 License.

References

Bang, W., Lee, G., Ryzhkov, A., Schuur, T., and Lim, K.-S. S.: Comparison of microphysical characteristics between the Southern Korean Peninsula and Oklahoma using two-dimensional video disdrometer data, Journal of Hydrometeorology, 21, 2675–2690, https://doi.org/10.1175/JHM-D-20-0087.1, 2020.

Berne, A., Jaffrain, J., and Schleiss, M.: Scaling analysis of the variability of the rain drop size distribution at small scale, Advances in water resources, 45, 2–12, https://doi.org/10.1016/j.advwatres.2011.12.016, 2012.

Byun, U.-Y., Hong, S.-Y., Shin, H., Lee, J.-W., Song, J.-I., Hahm, S.-J., Kim, J.-K., Kim, H.-W., and Kim, J.-S.: WRF-based short-range forecast system of the Korea Air Force: Verification of prediction skill in 2009 summer, Atmosphere, 21, 197–208, https://doi.org/10.14191/Atmos.2011.21.2.197, 2011.

Cha, J. W., Koo, H. J., Kim, B.-Y., Miloslav, B., Hwang, H. J., Kim, M. H., Chang, K.-H., and Lee, Y. H.: Analysis of rain drop size distribution to elucidate the precipitation process using a cloud microphysics conceptual model and in situ measurement, Asia-Pacific Journal of Atmospheric Sciences, 59, 257–269, https://doi.org/10.1007/s13143-022-00299-w, 2023.

Chakraborty, T., Pattnaik, S., Jenamani, R., and Baisya, H.: Evaluating the performances of cloud microphysical parameterizations in WRF for the heavy rainfall event of Kerala (2018), Meteorology and Atmospheric Physics, 133, 707–737, https://doi.org/10.1007/s00703-021-00776-3, 2021.

Chen, F. and Dudhia, J.: Coupling an advanced land surface–hydrology model with the Penn State–NCAR MM5 modeling system. Part I: Model implementation and sensitivity, Monthly weather review, 129, 569–585, https://doi.org/10.1175/1520-0493(2001)129%3C0569:CAALSH%3E2.0.CO;2, 2001.

Cohard, J. M. and Pinty, J. P.: A comprehensive two-moment warm microphysical bulk scheme. I: Description and tests, Quarterly Journal of the Royal Meteorological Society, 126, 1815–1842, https://doi.org/10.1002/qj.49712656613, 2000.

Dolan, B., Fuchs, B., Rutledge, S., Barnes, E., and Thompson, E.: Primary modes of global drop size distributions, Journal of the Atmospheric Sciences, 75, 1453–1476, https://doi.org/10.1175/JAS-D-17-0242.1, 2018.

Gao, W., Sui, C. H., Chen Wang, T. C., and Chang, W. Y.: An evaluation and improvement of microphysical parameterization from a two-moment cloud microphysics scheme and the Southwest Monsoon Experiment (SoWMEX)/Terrain-influenced Monsoon Rainfall Experiment (TiMREX) observations, Journal of Geophysical Research: Atmospheres, 116, https://doi.org/10.1029/2011JD015718, 2011.

Hagos, S., Leung, L. R., Yang, Q., Zhao, C., and Lu, J.: Resolution and dynamical core dependence of atmospheric river frequency in global model simulations, Journal of Climate, 28, 2764–2776, https://doi.org/10.1175/JCLI-D-14-00567.1, 2015.

Hersbach, H., Bell, B., Berrisford, P., Hirahara, S., Horányi, A., Muñoz-Sabater, J., Nicolas, J., Peubey, C., Radu, R., and Schepers, D.: The ERA5 global reanalysis, Quarterly Journal of the Royal Meteorological Society, 146, 1999–2049, https://doi.org/10.1002/qj.3803, 2020.

Hong, S.-Y., Noh, Y., and Dudhia, J.: A new vertical diffusion package with an explicit treatment of entrainment processes, Monthly weather review, 134, 2318–2341, https://doi.org/10.1175/MWR3199.1, 2006.

Iacono, M. J., Delamere, J. S., Mlawer, E. J., Shephard, M. W., Clough, S. A., and Collins, W. D.: Radiative forcing by long-lived greenhouse gases: Calculations with the AER radiative transfer models, Journal of Geophysical Research: Atmospheres, 113, https://doi.org/10.1029/2008JD009944, 2008.

Jiménez, P. A., Dudhia, J., González-Rouco, J. F., Navarro, J., Montávez, J. P., and García-Bustamante, E.: A revised scheme for the WRF surface layer formulation, Monthly weather review, 140, 898–918, https://doi.org/10.1175/MWR-D-11-00056.1, 2012.

Kain, J. S.: The Kain–Fritsch convective parameterization: an update, Journal of applied meteorology, 43, 170–181, https://doi.org/10.1175/1520-0450(2004)043%3C0170:TKCPAU%3E2.0.CO;2, 2004.

Kain, J. S. and Fritsch, J. M.: A one-dimensional entraining/detraining plume model and its application in convective parameterization, Journal of Atmospheric Sciences, 47, 2784–2802, https://doi.org/10.1175/1520-0469(1990)047%3C2784:AODEPM%3E2.0.CO;2, 1990.

Kwon, S., Jung, S.-H., and Lee, G.: A case study on microphysical characteristics of mesoscale convective system using generalized DSD parameters retrieved from dual-polarimetric radar observations, Remote Sensing, 12, 1812, https://doi.org/10.3390/rs12111812, 2020.

Lee, G., Bringi, V., and Thurai, M.: The retrieval of drop size distribution parameters using a dual-polarimetric radar, Remote Sensing, 15, 1063, https://doi.org/10.3390/rs15041063, 2023.

Lee, G. W., Zawadzki, I., Szyrmer, W., Sempere-Torres, D., and Uijlenhoet, R.: A general approach to double-moment normalization of drop size distributions, Journal of applied meteorology, 43, 264–281, https://doi.org/10.1175/1520-0450(2004)043%3C0264:AGATDN%3E2.0.CO;2, 2004.

Lim, K.-S. S. and Hong, S.-Y.: Development of an effective double-moment cloud microphysics scheme with prognostic cloud condensation nuclei (CCN) for weather and climate models, Monthly weather review, 138, 1587–1612, https://doi.org/10.1175/2009MWR2968.1, 2010.

Lim, K.-S. S. and Hong, S.-Y.: Investigation of aerosol indirect effects on simulated flash-flood heavy rainfall over Korea, Meteorology and Atmospheric Physics, 118, 199–214, https://doi.org/10.1007/s00703-012-0216-6, 2012.

Lin, Y.-L., Farley, R. D., and Orville, H. D.: Bulk Parameterization of the Snow Field in a Cloud Model, Journal of Applied

https://doi.org/10.5194/egusphere-2025-4548
Preprint. Discussion started: 20 February 2026
© Author(s) 2026. CC BY 4.0 License.

Meteorology and Climatology, 22, 1065–1092, https://doi.org/10.1175/1520-0450(1983)022<1065:BPOTSF>2.0.CO;2, 1983.
Meyers, M. P., Walko, R. L., Harrington, J. Y., and Cotton, W. R.: New RAMS cloud microphysics parameterization. Part II: The two-moment scheme, Atmospheric Research, 45, 3–39, https://doi.org/10.1016/S0169-8095(97)00018-5, 1997.
Min, K.-H., Choo, S., Lee, D., and Lee, G.: Evaluation of WRF cloud microphysics schemes using radar observations, Weather and Forecasting, 30, 1571–1589, https://doi.org/10.1175/WAF-D-14-00095.1, 2015.
Morcrette, J., Barker, H. W., Cole, J., Iacono, M. J., and Pincus, R.: Impact of a new radiation package, McRad, in the ECMWF Integrated Forecasting System, Monthly weather review, 136, 4773–4798, https://doi.org/10.1175/2008MWR2363.1, 2008.
Morrison, H.: On the robustness of aerosol effects on an idealized supercell storm simulated with a cloud system-resolving model, Atmospheric Chemistry and Physics, 12, 7689–7705, https://doi.org/10.5194/acp-12-7689-2012, 2012.
Morrison, H. and Milbrandt, J.: Comparison of Two-Moment Bulk Microphysics Schemes in Idealized Supercell Thunderstorm Simulations, Monthly Weather Review, 139, 1103–1130, https://doi.org/10.1175/2010MWR3433.1, 2011.
Morrison, H., Curry, J., and Khvorostyanov, V.: A new double-moment microphysics parameterization for application in cloud and climate models. Part I: Description, Journal of the atmospheric sciences, 62, 1665–1677, https://doi.org/10.1175/JAS3446.1, 2005.
Morrison, H., Kumjian, M. R., Martinkus, C. P., Prat, O. P., and van Lier-Walqui, M.: A general N-moment normalization method for deriving raindrop size distribution scaling relationships, Journal of Applied Meteorology and Climatology, 58, 247–267, https://doi.org/10.1175/JAMC-D-18-0060.1, 2019.
Morrison, H., Milbrandt, J. A., Bryan, G. H., Ikeda, K., Tessendorf, S. A., and Thompson, G.: Parameterization of cloud microphysics based on the prediction of bulk ice particle properties. Part II: Case study comparisons with observations and other schemes, Journal of the Atmospheric Sciences, 72, 312–339, https://doi.org/10.1175/JAS-D-14-0066.1, 2015.
Raupach, T. H., Thurai, M., Bringi, V., and Berne, A.: Reconstructing the drizzle mode of the raindrop size distribution using double-moment normalization, Journal of Applied Meteorology and Climatology, 58, 145–164, https://doi.org/10.1175/JAMC-D-18-0156.1, 2019.
Reisner, J., Rasmussen, R., and Bruintjes, R.: Explicit forecasting of supercooled liquid water in winter storms using the MM5 mesoscale model, Quarterly Journal of the Royal Meteorological Society, 124, 1071–1107, https://doi.org/10.1002/qj.49712454804, 1998.
Rutledge, S. A. and Hobbs, P.: The mesoscale and microscale structure and organization of clouds and precipitation in midlatitude cyclones. VIII: A model for the "seeder-feeder" process in warm-frontal rainbands, Journal of Atmospheric Sciences, 40, 1185–1206, https://doi.org/10.1175/1520-0469(1983)040%3C1185:TMAMSA%3E2.0.CO;2, 1983.
Schoenberg Ferrier, B.: A double-moment multiple-phase four-class bulk ice scheme. Part I: Description, Journal of Atmospheric Sciences, 51, 249–280, https://doi.org/10.1175/1520-0469(1994)051%3C0249:ADMMPF%3E2.0.CO;2, 1994.
Shin, K., Kim, K., Song, J. J., and Lee, G.: Polarimetric Retrieval of Raindrop Size Distribution: Double-Moment Normalization Approach and Machine Learning Techniques, Geophysical Research Letters, 51, e2023GL106057, https://doi.org/10.1029/2023GL106057, 2024.
Skamarock, W. C., Klemp, J. B., Dudhia, J., Gill, D. O., Liu, Z., Berner, J., Wang, W., Powers, J. G., Duda, M. G., and Barker, D. M.: A description of the advanced research WRF version 4, NCAR tech. note ncar/tn-556+ str, 145, https://www2.mmm.ucar.edu/wrf/users/docs/technote/v4_technote.pdf, 2019.
Song, H.-J. and Sohn, B.-J.: Two heavy rainfall types over the Korean peninsula in the humid East Asian summer environment: A satellite observation study, Monthly Weather Review, 143, 363–382, https://doi.org/10.1175/MWR-D-14-00184.1, 2015.
Sunny Lim, K.-S., Chang, E.-C., Sun, R., Kim, K., Tapiador, F. J., and Lee, G.: Evaluation of simulated winter precipitation using WRF-ARW during the ICE-POP 2018 field campaign, Weather and Forecasting, 35, 2199–2213, https://doi.org/10.1175/WAF-D-19-0236.1, 2020.
Testud, J., Oury, S., Black, R. A., Amayenc, P., and Dou, X.: The concept of "normalized" distribution to describe raindrop spectra: A tool for cloud physics and cloud remote sensing, Journal of Applied Meteorology, 40, 1118–1140, https://doi.org/10.1175/1520-0450(2001)040%3C1118:TCONDT%3E2.0.CO;2, 2001.
Thompson, G., Field, P. R., Rasmussen, R. M., and Hall, W. D.: Explicit forecasts of winter precipitation using an improved bulk microphysics scheme. Part II: Implementation of a new snow parameterization, Monthly weather review, 136, 5095–5115, https://doi.org/10.1175/2008MWR2387.1, 2008.
Torres, D. S., Porrà, J. M., and Creutin, J.-D.: A general formulation for raindrop size distribution, Journal of Applied Meteorology and Climatology, 33, 1494–1502, https://doi.org/10.1175/1520-0450(1994)033%3C1494:AGFFRS%3E2.0.CO;2, 1994.
Uijlenhoet, R., Steiner, M., and Smith, J. A.: Variability of raindrop size distributions in a squall line and implications for radar rainfall estimation, Journal of Hydrometeorology, 4, 43–61, https://doi.org/10.1175/1525-7541(2003)004%3C0043:VORSDI%3E2.0.CO;2, 2003.
Yang, Q., Dai, Q., Han, D., Chen, Y., and Zhang, S.: Sensitivity analysis of raindrop size distribution parameterizations in WRF rainfall simulation, Atmospheric Research, 228, 1–13, https://doi.org/10.1016/j.atmosres.2019.05.019, 2019.